



Nucleation mechanism of intra-granular blisters in tungsten exposed to hydrogen plasma

W.Q. Chen^{a,b}, X.Y. Wang^{a,*}, K.L. Li^a, Y.N. Wang^a, T.W. Morgan^c, B. Xu^a, Y.L. Chiu^{b,*}, W. Liu^{a,*}

^aSchool of Materials Science and Engineering, Tsinghua University, Beijing 100084, PR China

^bSchool of Metallurgy and Materials, University of Birmingham, Edgbaston, Birmingham B15 2TT, UK

^cDIFFER-Dutch Institute for Fundamental Energy Research, De Zaal 20, 5612 AJ Eindhoven, Netherlands

ARTICLE INFO

Article history:

Received 17 March 2020

Revised 4 June 2020

Accepted 5 June 2020

Available online 21 June 2020

Keywords:

Tungsten

Hydrogen plasma

Blisters

Nucleation mechanism

ABSTRACT

Despite being a subject of long-term research on fusion-reactor structural materials, the behaviour of hydrogen in tungsten under plasma exposure remains unclear. Here, the explicit transmission electron microscopy observations for recrystallised W after hydrogen plasma exposure are successfully obtained. These are the first observations to show the intra-granular blisters are located on the {100} planes. Molecular dynamics simulations confirm the hydrogen blister initiating at $\langle 100 \rangle$ dislocation core behaved similarly to those in experiment. We propose that the widely reported intra-granular hydrogen blisters are nucleated at the $\langle 100 \rangle$ edge dislocation core and develop along the {100} plane in tungsten.

© 2020 Acta Materialia Inc. Published by Elsevier Ltd. All rights reserved.

Nuclear fusion is considered as the most promising alternative to fossil fuel for a future carbon-free energy system. ITER, currently the largest fusion device under construction, is expected to produce a high heating power of ~ 150 MW [1]. However, the extreme environment created during ITER operation generates considerable challenges for the plasma-facing materials (PFMs) in the fusion-device divertor; e.g., high heat flux deposition and particle bombardment. Tungsten (W), having high thermal conductivity, high melting temperature, and low sputtering yield, is the most promising candidate PFM for use in an ITER divertor [2,3]. As a PFM, W is subject to low-energy (from tens to hundreds of electronvolts) bombardment from hydrogen (H) and its isotopes (deuterium (D) and tritium (T)), and high fluxes (10^{22} – 10^{24} ions/m² s). Such conditions induce formation of dome-shaped structures on the exposed surface, which are dubbed 'H blisters'. Examples of H blisters are shown in Fig. 1. H blisters cause dramatic degradation of W thermo-mechanical properties [4–6]. Therefore, understanding of W blistering behaviour is crucial for future development of materials that can withstand the extreme internal environment of a fusion reactor.

The relationship between the surface-observable H blisters and the subsurface H cavities has been confirmed from cross-sectional scanning electron microscopy (SEM) images [7–9]. Inter-granular blisters are believed to nucleate along grain boundaries [4,10].

However, the intra-granular blister nucleation mechanism remains unclear to date. Such nucleation is suspected to be associated with inter-granular defects, such as vacancies [11,12] or dislocations [10,13,14].

A vacancy can provide an iso-surface for collective H binding, causing H segregation and subsequent H blister nucleation [11]. However, due to the low vacancy concentration and plasma energy below displacement threshold, this mechanism cannot generate the H blisters observed in recrystallised W following low-energy H plasma exposure [4,8,10,15,16]. Previously, Fukai et al. [17–20] suggested the vacancy formation energy is decreased by the H-vacancy complex cluster ($V-H_n$) formation; this mechanism was used to explain the formation of super-abundant vacancies (SAV) in metals under high H pressure. However, Kong et al. [21] suggested the vacancy formation energy is decreased to ~ 2.45 eV by the $V-H_n$ complex formation; this is still very high and indicates that the vacancy concentration should remain extremely low (10^{-39} at room temperature). Finally, H blister formation at approximately room temperature has been reported. [16,22–24] But, at that temperature, vacancies or $V-H_n$ complexes are immobile (even with high concentration) and blisters cannot form.

Dislocations in W may serve as H traps. Thermal desorption spectroscopy (TDS) experiments have shown that increased dislocation density in W significantly increases the overall D retention [13]. Recent cryo-transfer atom probe tomography observations [25] also confirmed trapping of H by dislocations in body-centred cubic (bcc) iron (Fe). Thus, it is generally accepted that dislocations are H blister nucleation sites [14]. The binding energy

* Corresponding authors.

E-mail addresses: xiaoyang14@mails.tsinghua.edu.cn (X.Y. Wang), Y.Chiu@bham.ac.uk (Y.L. Chiu), liuw@tsinghua.edu.cn (W. Liu).

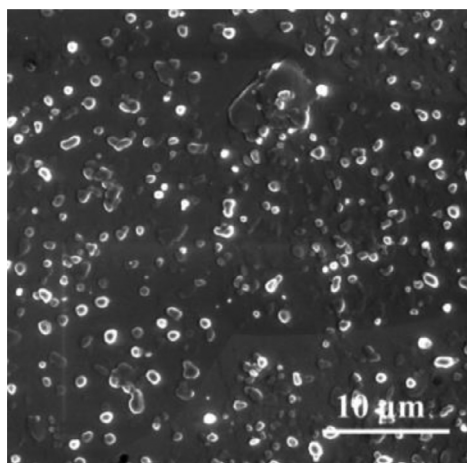


Fig. 1. SEM image of surface blistering morphology of W exposed to H plasma at 573 K.

between hydrogen atom and screw dislocation in tungsten is 0.55 eV [14], and for edge dislocation the binding energy is 0.89 eV [26]. In molecular dynamics (MD) simulations by Smirnov and Krashenninnikov [27], H can be trapped near either $1/2\langle 111 \rangle$ dislocations, forming platelet-shaped self-clusters, within which H atoms can accumulate to high concentrations. However, in those simulations, the accumulated H atoms did not eventually form an intra-granular H blister nucleus. Up to now, there is no direct evidence supporting $1/2\langle 111 \rangle$ dislocations are nucleation sites for hydrogen blisters.

Recently, Guo et al. [10] observed crack-shaped intra-granular blisters in recrystallised W after low-energy D plasma exposure. TEM revealed the existence of $\langle 001 \rangle$ dislocations with edge components alongside $\langle 111 \rangle$ edge dislocation interactions within dislocation tangles. Those researchers also found preferential blister formation in regions with high dislocation density. Following the crack nucleation theory suggested by Cottrell [28], i.e., a new $\langle 100 \rangle$ edge dislocation coalesced by two slip dislocations can serve as the nucleation site of a cleavage crack in deformed bcc metal, Guo et al. [10] speculated that a H crack could originate from a $\langle 100 \rangle$ edge dislocation with a similar mechanism. This crack would facilitate H platelet formation and eventually propagate by emitting $1/2\langle 111 \rangle$ edge dislocations. However, no evidence was provided to validate this H platelet formation mechanism in relation to dislocations and to confirm the development of H platelet clusters into H blisters. This is partly because of lacking information on H blister characterisation.

In this work, we utilise a focused ion beam (FIB) etching system combined with detailed transmission electron microscopy (TEM) observations to characterise H blisters and their associated microstructures [29,30]. Flash polishing following FIB lamella fabrication effectively removes FIB-damaged portions from the TEM foil. Along with the TEM observations, MD simulations are performed to elucidate the dislocation and H atom interaction, so as to reveal the detailed atomistic process of the early-stage H blister development.

Polycrystalline W with 99.99-wt% purity was supplied by Plansee Gruppe, Austria. After electro-polishing, all samples were heat-treated under vacuum at 1873 K for 2 h to obtain recrystallised W. The W samples were exposed to a high-flux H plasma beam in the Plasma-Surface Interaction (Magnum-PSI) linear plasma device (DIFFER, Eindhoven, the Netherlands), which allowed steady-state exposure of the target materials to ITER-relevant conditions [31]. The electron temperature and density were measured from the Thomson scattering data. The H plasma

flux was determined from the plasma beam temperature and controlled to $\sim 2 - 3 \times 10^{23} \text{ m}^{-2} \cdot \text{s}^{-1}$. The total fluence was $\sim 1.5 \times 10^{26} \text{ m}^{-2}$, and the ion energy was fixed $\sim 50 \text{ eV}$ by negatively biasing the sample. The temperature across the surface was set to $\sim 573 \text{ K}$. After the exposure, an Xe+ plasma-FIB system (FEI Helios G4 CXe) was utilised to extract TEM lamellae from the W surface; hence, cross-sectional foils parallel to the plasma exposure direction were obtained, with 20–40% less damage than that fabricated by Ga+ FIB [32,33]. To remove the damaged layers on both sides of the W lamellae resulting from the plasma-FIB process, a final flash-polishing procedure was performed at 14 V in a 0.5-wt% NaOH aqueous solution at 273 K for several milliseconds. TEM microstructural observations were performed using an FEI Talos F200 microscope operated at 200 kV under two-beam conditions in scanning TEM mode.

In the MD simulation, the X, Y, and Z directions were aligned along $\langle 100 \rangle$, $\langle 011 \rangle$, and $\langle 01\bar{1} \rangle$, with sizes of 50, 100, and 100 Å, respectively. Periodic boundary conditions were applied in the X and Y directions, and a free boundary condition was implemented in the Z direction. An $\langle 100 \rangle$ dislocation is created by the spontaneous merging of a $1/2\langle 11\bar{1} \rangle$ and a $1/2\langle 1\bar{1}1 \rangle$ edge dislocation, with line directions $\langle 011 \rangle$. Individual H atoms are introduced randomly in the system, followed by relaxation for 10 ps at 1000 K to facilitate H atom diffusion. This leads to an overall injection rate of $10^{26-27} \text{ m}^{-2} \cdot \text{s}^{-1}$, which was applied in other simulations such as Ref [27]. Although the injection rate is high, it still enables H atoms to enter the dislocation core and reach local equilibrium before they strongly interact with other H atoms, ensuring only one H cluster in the dislocation core to form nucleate of H blister. Thus, though the injection rate is 10^3 – 10^4 times higher than experiment due to timescale limitation of MD, it avoids qualitative difference to the overall nucleation behaviour and captures the essential physics of the nucleation process. During the simulation, a canonical ensemble was applied to maintain a constant temperature, atom number and volume. We chose two interatomic potentials for the W–H system developed by Bonny et al. [34] and one by Wang et al. [35], i.e., WHHe1, WHHe2, and Wang WH, respectively. The MD simulation was implemented using the LAMMPS [36] code, and the simulation results were visualised using the OVITO [37] software.

Cross-sectional views of the recrystallised W microstructure after exposure to high-flux, low-energy H plasma at 573 K are shown in Fig. 2. Fig. 2a shows an overview of the near-surface. Fig. 2b–d are enlarged views of Areas 1–3, respectively, which are marked by red rectangles in Fig. 2a. The foil normal of each sample was near $[011]$. The target areas were observed for different two-beam conditions and zone axes. The images of Areas 1–3 reveal H blisters on the (100) , (001) , and (010) planes, respectively. Other typical blisters located near the exposure surface in Fig. 2a were also found to be located on the $\{100\}$ planes (see Supplementary Fig. 1 and Supplementary Material 1). This is the first cross-section observation showing H blister has strong orientation dependence in W after plasma exposure.

Fig. 3 shows examples of dislocations and dislocation tangles that formed in the recrystallised W following H plasma exposure. The overall location of the areas shown in Fig. 3 is marked by a white rectangle in Supplementary Fig. 2. The typical dislocations labelled **a** and **b** and marked by yellow lines (dotted and solid lines are used for invisible and visible dislocations, respectively) in Fig. 3 were analysed under two-beam conditions. The foil normal of the W sample was near $[313]$. Typical Burgers vectors **b** of W dislocations are of $\pm a\langle 001 \rangle$ and $\pm a/2\langle 111 \rangle$ type [38,39]. According to the $g \cdot b = 0$ invisibility criterion, where **b** is the Burgers vector length, the Burgers vectors of the type **a** and **b** dislocations in Fig. 3 are $\mathbf{b}_a = \mathbf{b}_b = \pm[001]$. The dislocation lines, $\mathbf{u}_a = \pm[100]$ and $\mathbf{u}_b = \pm[1\bar{1}0]$, are perpendicular to the Burgers

vector and satisfy $g \cdot b \times u = 0$; thus, **a** and **b** are edge dislocations. In a bcc lattice, a $[001]$ edge dislocation can only be created when two slip dislocations coalesce to lower their elastic energy, i.e., $\frac{a}{2}[111] + \frac{a}{2}[\bar{1}\bar{1}\bar{1}] \rightarrow a[001]$ [28]. An analogous observation of $\pm a\langle 001 \rangle$ edge dislocation has recently been reported in Ref. [10]; that report validates the existence of $\pm a\langle 001 \rangle$ edge dislocation during H plasma exposure.

To understand the nucleation mechanism, an MD simulation was performed to study the behaviour of increasing H concentration near $\langle 100 \rangle$ edge dislocations core. Such process is shown in Fig. 4. Initial configuration of the edge dislocation is shown in Fig. 4a. With the gradual increase of hydrogen density near the dislocation, the core structure of the $\langle 100 \rangle$ edge dislocation was saturated with H. The saturation was validated using Molecular Statics calculation and a Mean-Field theory model [40] provided in Supplementary Materials 2 and 3. A cascade effect is triggered that H atoms drives the dislocation core open towards the $\langle 011 \rangle$ direction, and more H atom is captured by the open dislocation core. This behaviour is similar to crack nucleation process in Cottrell's theory [28]. However, in the present study, the driving force

for the blister formation and early stage development was H atom absorption, rather than an external load.

Simultaneously, an H-rich phase-transition region formed near the tip of the opened core, as shown in Fig. 4b–f. An enlarged image showing the detailed structure of the phase-transition region is shown in Fig. 4d. Within the H-rich region, the W atoms formed a face-centred cubic structure, as determined from common neighbour analysis [41]. The structure of this region is consistent with the previously reported H self-trapping structure in W [27]. Phase-transition region formed when WHHe1 and Wang WH is applied. Another potential, WHHe2 [34] failed to produce the phase-transition structure, presumably because of its less accurate H–H interaction [35]. The formation of a H-rich phase-transition region near the tip of a crack-shape defect was also observed for bcc Fe [42], in which such region was introduced by the stress concentration near a crack under external load, which is absent in the present study. Similar H-rich regions near $1/2\langle 111 \rangle$ screw and edge dislocations were also observed in MD simulations performed by Smirnov et al. [27]. However, H accumulation at a $1/2\langle 111 \rangle$ dislocation does not eventually induce H blister formation. This

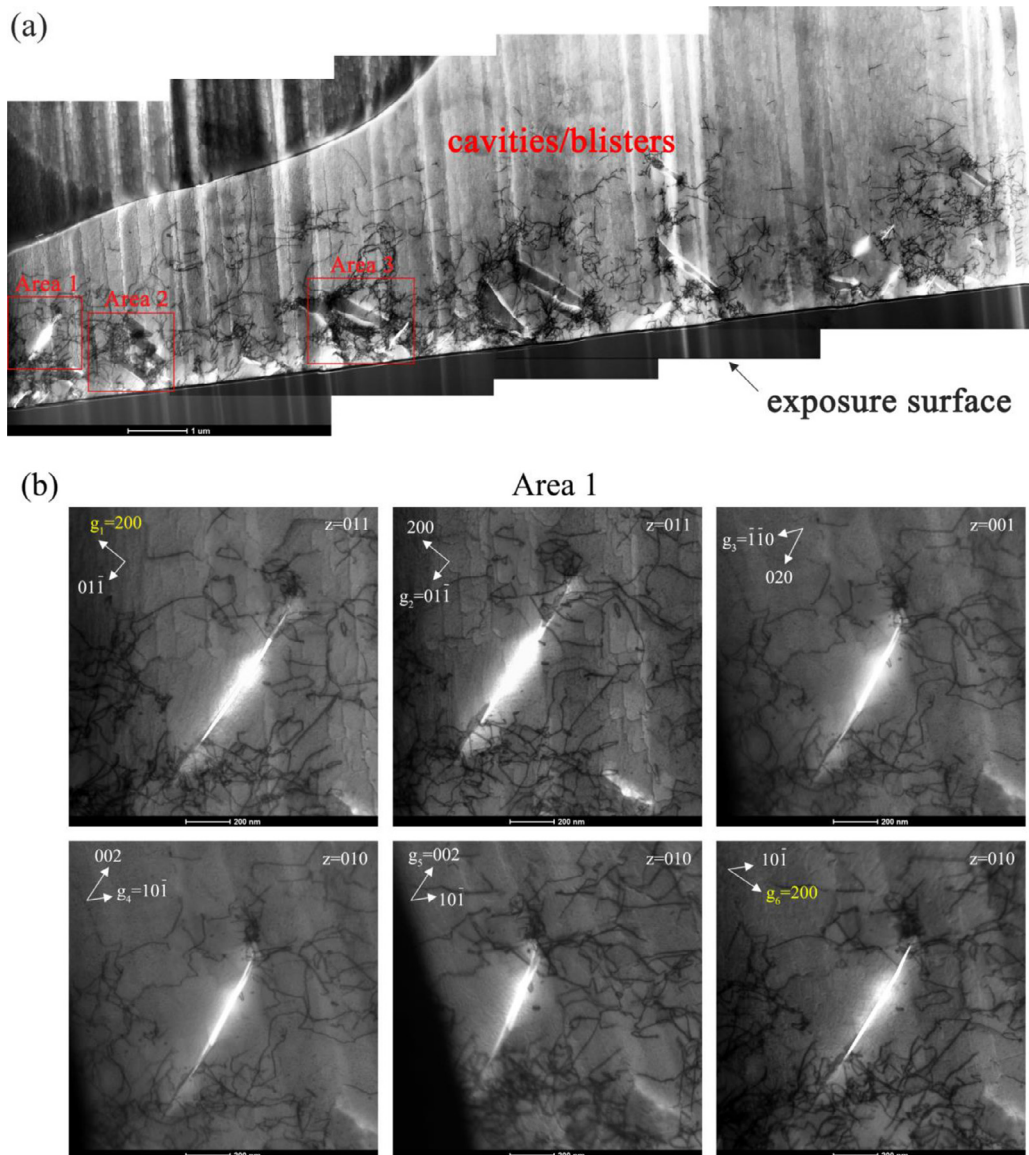


Fig. 2. TEM images of W microstructures following exposure to H plasma at 573 K. (a) Overview of H blisters/cavities distributed at near-surface, with numerous surrounding dislocations. (b)–(d) Enlarged images of Areas 1–3 in (a), showing H blisters located in the (100), (001), and (010) planes, respectively.

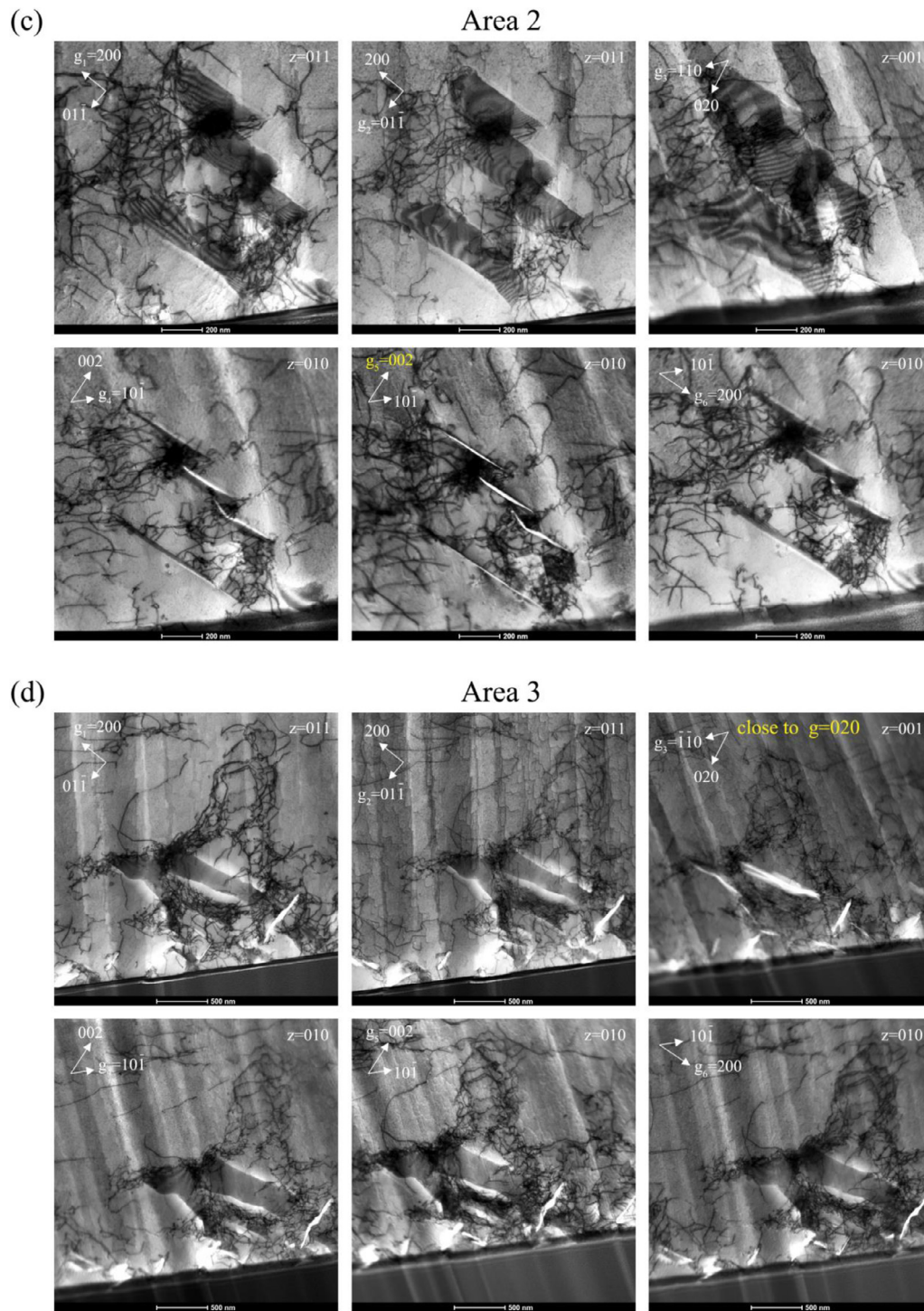


Fig. 2. Continued

difference may exist because a $\langle 100 \rangle$ dislocation has a stronger tendency to attract H atoms because of its high binding energy. The resultant H-enriched $\langle 100 \rangle$ -type dislocation cores may serve as nucleation sites for intra-granular H blisters.

Opened dislocation core would then develop into a H-filled cavity. With H atoms gradually entering the cavity, the cavity extends further in the $\langle 011 \rangle$ direction. As shown in Fig. 4b–f, the phase-transition region is always associated with the cavity tip, which indicates that the H-rich phase-transition region is induced by the stress field near the cavity tip. Meanwhile, as shown in Fig. 4c–e,

the phase-transition region expands as the open volume extends, because the stress field becomes stronger with the blister growth.

We next analysed the H diffusion path. As shown in Fig. 4e, the H diffused randomly until it entered the H-rich phase-transition region. Furthermore, we find most H atoms in the phase-transition region entered the cavity. As the phase-transition region followed the cavity tip, we suspect that this region is in an intermediate state prior to H in-blisters absorption.

We then examined whether a screw dislocation observed in previous literature [10], could also trigger the nucleation of H.

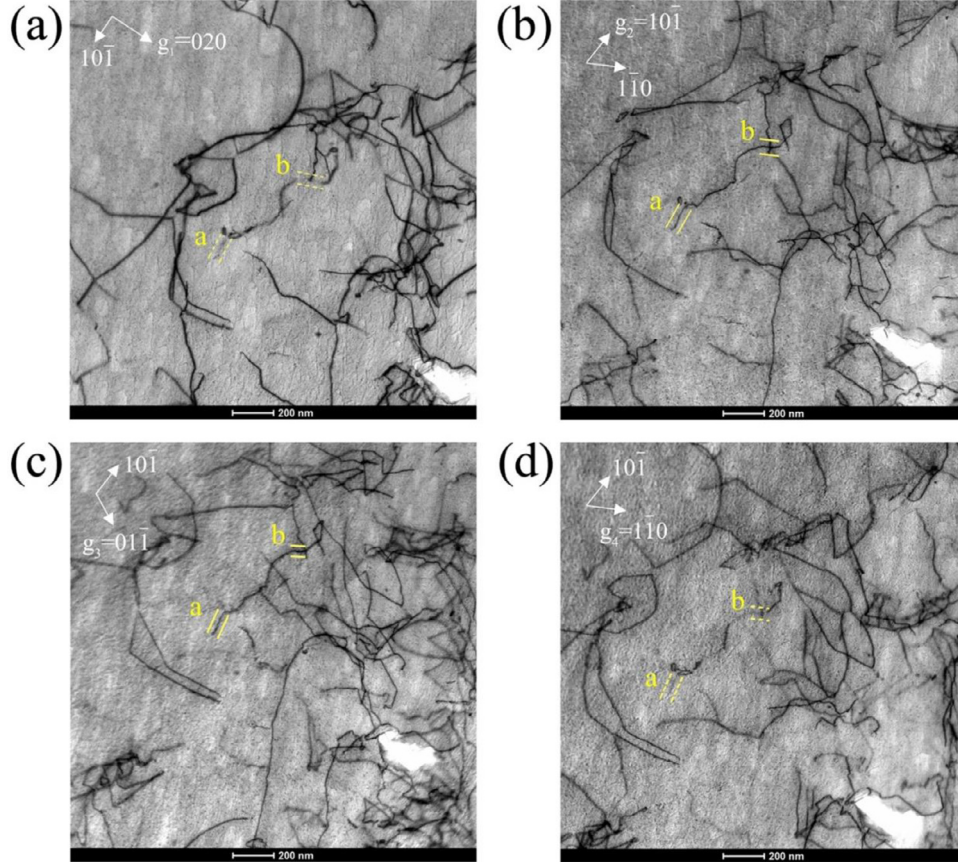


Fig. 3. Two-beam-condition TEM images of dislocations, from which Burgers vectors \mathbf{b} were identified using the $\mathbf{g} \cdot \mathbf{b} = 0$ criterion. The identified dislocations, labelled ‘a’ and ‘b’, are depicted by straight or dotted lines, for visible or invisible dislocations, respectively. The Burgers vectors of the type \mathbf{a} and \mathbf{b} dislocations are $\mathbf{b}_a = \mathbf{b}_b = [001]$. The directions of the dislocation lines $\mathbf{u}_a = \pm[100]$, $\mathbf{u}_b = \pm[1\bar{1}0]$ are perpendicular to \mathbf{b} and satisfy $\mathbf{g} \cdot \mathbf{b} \times \mathbf{u} = 0$ (where b is the Burgers vector length), indicating that \mathbf{a} and \mathbf{b} are edge dislocations. The location of the analysed area is marked by a white rectangle in Supplementary Fig. 2.

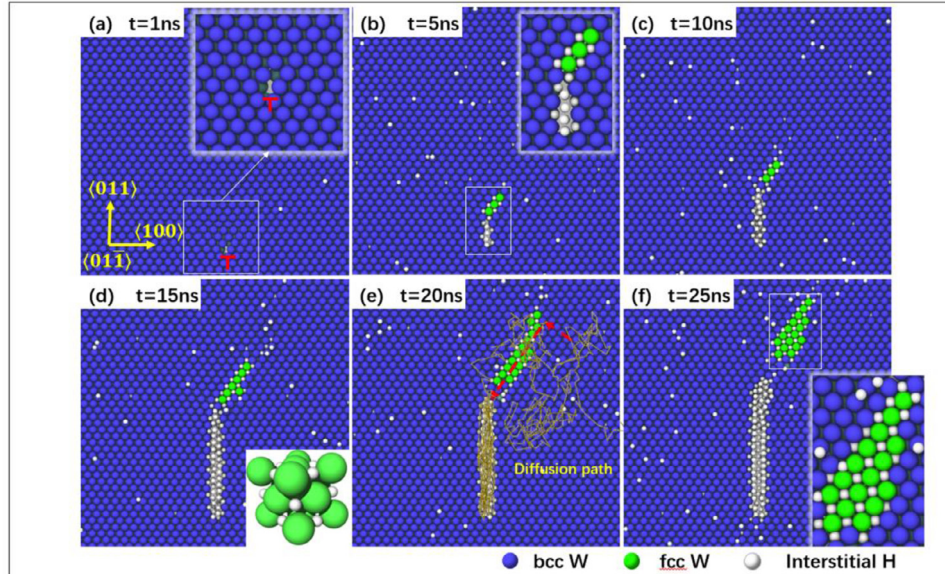


Fig. 4. H-blister nucleation process at dislocations. (a) At $t = 1$ ns, the edge dislocation with a $\langle 100 \rangle$ Burgers vector is not filled by H atoms. The enlarged figure shows the dislocation core structure. (b) At $t = 5$ ns, the dislocation core opens towards the $\langle 011 \rangle$ direction and accommodates more H atoms. The H-rich phase-transformation region is also formed at this stage. (c) At $t = 10$ ns, the dislocation core extends further. (d) At $t = 15$ ns, with increased blister size, the phase-transformation region increases. The enlarged figure shows the crystal structure of the phase-transformation region, which is fcc W with H filling all of its octahedral sites. (e) At $t = 20$ ns, the H dislocation diffusion path is visible. (f) At $t = 25$ ns, the final configuration is apparent; the phase-transformation region grows continuously, following the blister tip.

We repeated the above simulation with a $\langle 100 \rangle$ screw dislocation, and WHHe1 potential was employed in this simulation. The results indicate that H atoms accumulating near a screw dislocation can only form a platelet-like H self-cluster, with the H atoms occupying octahedron interstitial sites. These different H behaviours at the $\langle 100 \rangle$ edge and screw dislocations can be attributed to their various associated stress fields. Edge and screw dislocations have stronger normal (tensile or compressive) and shear stress components, respectively. Lu and coworkers [43] suggests, normal stress, whether compressive or tensile, can increase H solubility in W. Thus, edge dislocations are expected to attract more H atoms than screw dislocations for the same overall H concentration.

Note that the MD simulation result only provides reliable support for the proposed nucleation mechanism for intra-granular H blisters. The H-filled planar shape blister further develops into a larger H blister, and the growth mechanism may change in later stages of the blister growth to involve loop punching [44] or dislocation emission [10,45].

Based on the experiment results and MD simulation, the H blister nucleation process can be summarised as follows:

1. Dislocation entangle forms in areas that have strong thermal gradient. $\langle 100 \rangle$ dislocations form in these entangles.
2. The binding strength and large capacity of a $\langle 100 \rangle$ dislocation enables it to capture significant amount of H solutes.
3. The saturated H atom in the dislocation core drives it open towards tensile stress field, creating additional capacity for more H atoms. A phase transition region is created following the opening dislocation core, providing intermediate accommodation for H atoms. This process causes initial nucleation of a H blister, a crack-shaped structure perpendicular to the $\langle 100 \rangle$ direction.

In summary, we investigated the nucleation mechanism of H blisters in W exposed to high-flux, low-energy H plasma. We obtained explicit cross-sectional TEM views of the sample morphology and, remarkably, confirmed the presence of $\langle 001 \rangle$ edge dislocations and the preference for $\{100\}$ planes by all H crack-shaped blisters. Based on MD simulation, we derived a reliable H blister nucleation mechanism. This study provides new insights into the underlying effects of H plasma exposure in PFMs, which are of vital importance for further development of nuclear fusion technology.

Declaration of Competing Interest

The authors declare that they have no known competing financial interests or personal relationships that could have appeared to influence the work reported in this paper.

Acknowledgements

This work was supported by the National Nature Science Foundation of China under Contract No. 51971115, and the Tsinghua Scholarship for Overseas Graduate Studies. This work was performed within the framework of the EURO Fusion Consortium and received funding from the [Euratom research and training programme](#) (2014–2018 and 2019–2020) under grant agreement No. 633053. The views and opinions expressed herein do not necessarily reflect those of the European Commission. DIFFER is a partner of the Trilateral Euregio Cluster (TEC). Technical support from the Centre for Electron Microscopy of the University of Birmingham, U.K., is acknowledged. W. Q. Chen is grateful for valuable support with TEM and plasma-FIB techniques provided by Dr. Shanshan Si, Dr. Minshi Wang, and Dr. Xinyu Lu at the University of Birmingham, and for support with flash polishing supplied by Dr. Robin

Schaeublin of ETHZ Switzerland. The assistance of Mr. Wangguo Guo at Beihang University is also gratefully acknowledged.

Supplementary material

Supplementary material associated with this article can be found, in the online version, at doi:[10.1016/j.scriptamat.2020.05.054](https://doi.org/10.1016/j.scriptamat.2020.05.054).

References

- [1] A. Kallenbach, M. Bernert, R. Dux, L. Casali, T. Eich, L. Giannone, A. Herrmann, R. McDermott, A. Mlynec, H.W. Muller, F. Reimold, J. Schweinzer, M. Sertoli, G. Tardini, W. Treutler, E. Viezer, R. Wenninger, M. Wischmeier, A.U. Team, *Plasma Phys. Control Fusion* 55 (12) (2013) 10.
- [2] T. Hirai, F. Escourbiac, S. Carpentier-Chouchana, A. Durocher, A. Fedosov, L. Ferland, T. Jokinen, V. Komarov, M. Merola, R. Mitteau, R.A. Pitts, W. Shu, M. Sugihara, V. Barabash, V. Kuznetsov, B. Riccardi, S. Suzuki, *Phys. Scr. T159* (2014) 014006.
- [3] G. De Temmerman, T. Hirai, R.A. Pitts, *Plasma Phys. Control Fusion* 60 (2018) 044018.
- [4] W.Q. Chen, X.Z. Xiao, B. Pang, S.S. Si, Y.Z. Jia, B. Xu, T.W. Morgan, W. Liu, Y.L. Chiu, *J. Nucl. Mater.* 522 (2019) 11–18.
- [5] M. Nagumo, *Fundamentals of Hydrogen Embrittlement*, Springer-Verlag Singapore Pte Ltd, Singapore, 2016.
- [6] J. Roth, K. Schmid, *Phys. Scr. T145* (2011) 9.
- [7] Y.Z. Jia, G. De Temmerman, G.N. Luo, H.Y. Xu, C. Li, B.Q. Fu, W. Liu, *J. Nucl. Mater.* 457 (2015) 213–219.
- [8] W.M. Shu, *Appl. Phys. Lett.* 92 (21) (2008) 211904.
- [9] M. Balden, S. Lindig, A. Manhard, J.-H. You, *J. Nucl. Mater.* 414 (1) (2011) 69–72.
- [10] W. Guo, L. Ge, Y. Yuan, L. Cheng, S. Wang, X. Zhang, G.-H. Lu, *Nucl. Fusion* 59 (2019) 026005.
- [11] Y.L. Liu, Y. Zhang, H.B. Zhou, G.H. Lu, F. Liu, G.N. Luo, *Phys. Rev. B* 79 (17) (2009) 172103.
- [12] W.T. Geng, L. Wan, J.P. Du, A. Ishii, N. Ishikawa, H. Kimizuka, S. Ogata, *Scr. Mater.* 134 (2017) 105–109.
- [13] D. Terentyev, G. De Temmerman, T.W. Morgan, Y. Zayachuk, K. Lambrinou, B. Minov, A. Dubinko, K. Bystrov, G. Van Oost, *J. Appl. Phys.* 117 (8) (2015) 083302.
- [14] D. Terentyev, V. Dubinko, A. Bakaev, Y. Zayachuk, W. Van Renterghem, P. Grigorev, *Nucl. Fusion* 54 (4) (2014) 042004.
- [15] W.M. Shu, E. Wakai, T. Yamanishi, *Nucl. Fusion* 47 (3) (2007) 201–209.
- [16] W.M. Shu, A. Kawasuso, Y. Miwa, E. Wakai, G.N. Luo, T. Yamanishi, *Phys. Scr. T128* (2007) 96–99.
- [17] Y. Fukai, N. Okuma, *Phys. Rev. Lett.* 73 (12) (1994) 1640–1643.
- [18] Y. Fukai, Y. Ishii, Y. Goto, K. Watanabe, *J. Alloy Compd.* 313 (2000) 121–132.
- [19] Y. Fukai, *J. Alloy Compd.* 356 (2003) 263–269.
- [20] H. Sugimoto, Y. Fukai, *Scr. Mater.* 134 (2017) 20–23.
- [21] X.S. Kong, Y.W. You, Q.F. Fang, C.S. Liu, J.L. Chen, G.N. Luo, B.C. Pan, Z.G. Wang, *J. Nucl. Mater.* 433 (1–3) (2013) 357–363.
- [22] Y.K. Alimov, W.M. Shu, J. Roth, K. Sugiyama, S. Lindig, M. Balden, K. Isobe, T. Yamanishi, *Phys. Scr. T138* (2009) 014048.
- [23] G.N. Luo, W.M. Shu, M. Nishi, *Fusion Eng. Des.* 81 (8–14) (2006) 957–962.
- [24] V.K. Alimov, B. Tyburska-Püschel, S. Lindig, Y. Hatano, M. Balden, J. Roth, K. Isobe, M. Matsuyama, T. Yamanishi, *J. Nucl. Mater.* 420 (1–3) (2012) 519–524.
- [25] Y.-S. Chen, H. Lu, J. Liang, A. Rosenthal, H. Liu, G. Sneddon, I. McCarroll, Z. Zhao, W. Li, A. Guo, J.M. Cairney, *Phys. Scr.* 367 (6474) (2020) 171–175.
- [26] A. Bakaeva, D. Terentyev, G. De Temmerman, K. Lambrinou, T.W. Morgan, A. Dubinko, P. Grigorev, K. Verbeken, J.M. Noterdaeme, *J. Nucl. Mater.* 479 (2016) 307–315.
- [27] R.D. Smirnov, S.I. Krashennnikov, *Nucl. Fusion* 58 (12) (2018) 126016.
- [28] A.H. Cottrell, *Trans. Am. Inst. Min. Metall. Eng.* 212 (1958) 192–203.
- [29] A. Manhard, U. von Toussaint, M. Balden, S. Elgeti, T. Schwarz-Selinger, L. Gao, S. Kapser, T. Płociński, J. Grzonka, M. Gloc, Ł. Ciupiński, *Nucl. Mater. Energy* 12 (2017) 714–719.
- [30] M. Rasinski, A. Kreter, Y. Torikai, C. Linsmeier, *Nucl. Mater. Energy* 12 (2017) 302–306.
- [31] H.J.N. van Eck, G.R.A. Akkermans, S.A. van der Westen, D.U.B. Aussems, M. van Berkel, S. Brons, I.G.J. Classen, H.J. van der Meiden, T.W. Morgan, M.J. van de Pol, J. Scholten, J.W.M. Vernimmen, E.G.P. Vos, M.R. de Baar, *Fusion Eng. Des.* 142 (2019) 26–32.
- [32] R.D. Kelley, K. Song, B. Van Leer, D. Wall, L. Kwakman, *Microsc. Microanal.* 19 (S2) (2013) 862–863.
- [33] T.L. Burnett, R. Kelley, B. Winiarski, L. Contreras, M. Daly, A. Gholinia, M.G. Burke, P.J. Withers, *Ultramicroscopy* 161 (2016) 119–129.
- [34] G. Bonny, P. Grigorev, D. Terentyev, *J. Phys. Condens.* 26 (48) (2014) 485001.
- [35] L.F. Wang, X. Shu, G.H. Lu, F. Gao, *J. Phys. Condens.* 29 (43) (2017) 435401.
- [36] S. Plimpton, *Fast Parallel Algorithms for Short-Range Molecular Dynamics*, Sandia National Labs., Albuquerque, NM, United States, 1993.
- [37] S. Alexander, *Model. Simul. Mater. Sci.* 18 (1) (2010) 015012.
- [38] T. Tabata, H. Mori, H. Fujita, I. Ishikawa, *J. Phys. Soc. Jpn.* 40 (4) (1976) 1103–1111.
- [39] C.Y. Chiem, W.S. Lee, *Mater. Sci. Eng. A: Struct. Mater. Prop. Microstruct. Process.* 187 (1) (1994) 43–50.

- [40] L. Ventelon, B. Lüthi, E. Clouet, L. Proville, B. Legrand, D. Rodney, F. Willaume, Phys. Rev. B 91 (22) (2015) 220102(R).
- [41] A. Stukowski, Model. Simul. Mater. Sci. 20 (4) (2012) 045021.
- [42] J. Song, W.A. Curtin, Nat. Mater. 12 (2) (2012) 145–151.
- [43] H.B. Zhou, S. Jin, Y. Zhang, G.H. Lu, F. Liu, Phys. Rev. Lett. 109 (13) (2012) 135502.
- [44] R.D. Kolasinski, D.F. Cowgill, D.C. Donovan, M. Shimada, W.R. Wampler, J. Nucl. Mater. 438 (2013) S1019–S1022.
- [45] J. Hou, X.S. Kong, X.B. Wu, J. Song, C.S. Liu, Nat. Mater. 18 (8) (2019) 833–839.